



In-situ pyrolysis of *Enteromorpha* as carbocatalyst for catalytic removal of organic contaminants: Considering the intrinsic N/Fe in *Enteromorpha* and non-radical reaction

Cheng Chen^a, Tengfei Ma^a, Yanan Shang^a, Baoyu Gao^{a,*}, Bo Jin^b, Hongbing Dan^a, Qian Li^a, Qinyan Yue^a, Yanwei Li^c, Yu Wang^d, Xing Xu^{a,*}

^a Shandong Key Laboratory of Water Pollution Control and Resource Reuse, School of Environmental Science and Engineering, Shandong University, Jinan, 250100, PR China

^b School of Chemical Engineering, University of Adelaide, Australia

^c Environment Research Institute, Shandong University, Jinan, 250100, PR China

^d Shandong Construction Project Environmental Assessment Service Center, PR China

ARTICLE INFO

Keywords:

Enteromorpha
Non-radical reaction
Graphitic N
Paracetamol
DFT

ABSTRACT

An environmentally friendly, facile, and economical Fe/N co-doped carbonaceous material (Fe-N@C) was prepared by the in-situ pyrolysis of Fe/N rich *Enteromorpha* biomass for peroxymonosulfate activation and organic contaminants degradation. Results indicated that *Enteromorpha*-based catalysts prepared at high pyrolysis temperature displayed some highly graphitic nanosheets with rich nitrogen doped. The graphitic N derived from the intrinsic N in *Enteromorpha* showed the high correlation with the paracetamol (PCM) removal rate; this was confirmed by the Density Functional Theory (DFT) calculation, showing the high adsorption energy (ΔE_{ads} , -2.62 eV) of PMS molecular adsorbed onto the graphitic N area. A weak correlation between the PCM removal rate and adsorption capacity was also observed, revealing that the PCM catalytic reaction could be greatly accelerated after the pre-adsorption. It was interesting that the intrinsic Fe in *Enteromorpha* did not affect the PCM degradation, but PCM removal rate of acid treated Fe-N/C was improved as more active sites were formed after the Fe extraction by acid treatment. Both the radical pathways of $\text{O}_2^{\cdot-}$ and non-radical $^1\text{O}_2$ generated in the Fe-N@C/PMS system were the primary mechanisms for the PCM degradation, which was consistent with the Fukui function values of f^+ and f^- based on the DFT calculation. In addition, high stability of the carbon-based catalysts was observed after three runs and calcinating regeneration, which showed the promising applications for environmental remediation.

1. Introduction

The pharmaceuticals and personal care products (PPCPs) in natural waters has received increasing concerns in recent decades because of their adverse effect on health and aquatic environment [1–5]. As one of the most common PPCPs, paracetamol (PCM) is widely used for treating the headache, arthralgia, and fever in adults and children [6,7]. Due to its persistence in the receiving environment and inefficacy by biological treatment, the accumulation of PCM in lakes, rivers, groundwater and even drinking water has been detected, which results in harmful consequences for ecosystem and human health [8,9].

Advanced oxidation processes (AOPs) are receiving more concerns for in situ destruction of PCM in aquatic environment [9–13]. Most reported work was based on the forms of reactive hydroxyl radicals

($\cdot\text{OH}$) in different systems [14]. Over the last decade, sulfate radical ($\text{SO}_4^{\cdot-}$) based AOPs are considered to be the innovative oxidative treatment for the organic contaminants in water. The $\text{SO}_4^{\cdot-}$ could be activated from persulfates, e.g. peroxymonosulfate (PMS) and peroxydisulfate (PDS), which exerted several advantages with respect to $\cdot\text{OH}$, such as higher redox potential (2.5–3.1 V) and higher life time (30–40 μs) [15].

Persulfates activated by a series of transition metal ions (Cu^{2+} , Co^{2+} , Fe^{2+} , Ni^{+} , and Ce^{3+}) or metal oxides (Co_3O_4 , MnO_2 , FeMnO_x) were reported to be effective to generate the sulfate radicals [16–19]. However, the inevitable metal leaching into environment caused irreversible catalytic deactivation reaction and secondary pollution, which greatly restricted their practical applications in field. More recently, carbon materials (e.g. CNTs, GO, and activated carbon) emerged as

* Corresponding authors.

E-mail addresses: baoyugao_sdu@aliyun.com (B. Gao), xuxing@sdu.edu.cn (X. Xu).

<https://doi.org/10.1016/j.apcatb.2019.03.048>

Received 17 January 2019; Received in revised form 14 March 2019; Accepted 16 March 2019

Available online 20 March 2019

0926-3373/ © 2019 Elsevier B.V. All rights reserved.

promising alternatives for PMS activation due to their intrinsic open and sp^2 -hybridized carbon matrix with versatile catalytic groups and edges [20–25]. Although they could greatly alleviate metal leaching issues, the catalytic performances of these metal-free catalysts were still unsatisfactory and the exact nature of the catalytic sites in the carbon matrix is still controversial [22]. As a result, enormous studies have focused on the carbon matrix with N or metal doped, which could form more catalytic sites for enhancing the carbocatalysis [15,19,26–29]. Long et al. prepared the N-doped hierarchically porous carbon using tannic acid and dicyandiamide [30]. Yao et al. further fabricated multiple metal encapsulated nitrogen-doped carbon nanotubes using dicyandiamide and salts of metal [31]. The enhanced active sites in the composites were ascribed to the nitrogen-doped carbon and encapsulated metal nanoparticles in the carbon matrix, and the encapsulated metal nanoparticles can also be protected from leaching [31]. However, fabrication of these carbon-based materials always required complicated synthesis routes and synthetic reagents with high costs, which would confine their further application at the current stage [23].

Enteromorpha is a kind of green algae, which is rich in nitrogenous compounds, e.g. polysaccharides, proteins and vitamins [32,33]. In addition, high amounts of Fe (0.2–0.5 wt %) in *Enteromorpha* were also reported [34]. As a result, fascinating strategy using both the high amounts of N and Fe in the *Enteromorpha* as alternatives to be co-doped into the carbonaceous material after in-situ pyrolysis of *Enteromorpha* was proposed, which attempted to form the “green” catalyst for the destruction of organics. In addition, it should be pointed that the biomass after in-situ pyrolysis always endowed with considerable pore structures and abundant surface groups for organic molecules adsorption [23]. As a result, the adsorptive and catalytic performances of *Enteromorpha* derived carbonaceous material should be evaluated.

In this work, we reported an environmentally friendly, facile, economical, and fascinating process for fabricating the N and Fe co-doped carbonaceous material (Fe-N@C) by the thermal treatment of *Enteromorpha* biomass. PCM catalytic performances considering the roles of intrinsic N and Fe in the *Enteromorpha* were evaluated. The adsorptive and catalytic performances of some other biomass-based catalysts were also presented. The underlying mechanism for the degradation of PCM in PMS/Fe-N@C system was particularly concerned according to the Density Functional Theory (DFT).

2. Materials and methods

2.1. Chemicals

The *Enteromorpha* was obtained from Qingdao (36.10 N, 120.51 E), Shandong Province in China. The pristine *Enteromorpha* biomass was first washed with tap water, dried in air and then sieved into powders with size of 250–500 μm . The chemicals, including KOH, H_2SO_4 , NaOH, NaH_2PO_4 , Na_2SO_4 , NaCl, NaHCO_3 , humic acid and HCl (32%–37%) were obtained from Sinopharm Chemical Reagent Co. Ltd. The potassium peroxydisulfate (PMS), 5,5-dimethyl-1-pyrroline-N-oxide (DMPO), 2,2,6,6-Tetramethyl-4-piperidone (4-oxo-TEMP), ethanol (EtOH), *tert*-butyl alcohol (TBA), *p*-benzoquinone (*p*-BQ) and *L*-histidine were provided from Sigma-Aldrich.

2.2. Fabrication of Fe-N@C catalysts from *Enteromorpha*

The carbonization of *Enteromorpha* biomass (5.0 g) was first carried out in N_2 atmosphere in a tube furnace at temperature of 500 °C for 1.5 h. The carbonized *Enteromorpha* biomass was then collected after cooling to ambient temperature. Then, approximately 3.0 g of carbonized *Enteromorpha* was mixed with 1.5 g of KOH. The mixture was placed on the combustion boat and annealed in a tube furnace for 60 min under the nitrogen atmosphere. The annealing temperatures were designed in the range of 600–900 °C with rate of 5 °C min^{-1} . After

cooling, the Fe-N@C catalysts prepared at different temperatures (600, 700, 800 and 900 °C) were ground, washed with deionized water repeatedly, dried and stored before use. To test the adsorptive and catalytic capacity of Fe-N@C after acid treatment, sample of Fe-N@C 700 was mixed with 1 M H_2SO_4 for 10 h (80 °C). The sample was washing with deionized water and ethanol. It was then collected after drying in an oven. Other typical biomass (e.g. soybean, *spirulina*, bean stalk, and kelp) were also fabricated into the catalysts as above procedures. Characterization of the pristine, carbonized *Enteromorpha* biomass as well as multiple Fe-N@C catalysts was presented in Supporting file.

2.3. PCM adsorption and degradation tests

Unless stated otherwise, all the PCM degradation tests were conducted by mixing 5 mg of catalysts, 0.5 mM of PMS and 50 mL of PCM solution (10 mg/L) in 125 mL of Erlenmeyer flask. The pH of suspension was controlled at 5.6 with the stirring at 300 rpm. As the reaction was initiated, 1 mL of sample was withdrawn and filtered using the 0.22 μm film. Then the reaction was quenched by adding 0.5 mL of methanol. The residual PCM in the resultant solution was determined by a high-performance liquid chromatograph (HPLC, UltiMate 3000) with a C-18 column. PCM degradation at different Fe-N@C dosages (0.02–0.1 g/L), PMS dosages (0.15–1.0 mM), and pH conditions (3.6–10.5) was evaluated. PCM degradation in Fe-N@C/PMS system considering the co-existing Cl^- , HCO_3^- , H_2PO_4^- , and humic acid (HA) was also determined. The catalytic quenching reactions were conducted by adding different quenching agents, e.g. EtOH, TBA, *p*-BQ and *L*-histidine into the Fe-N@C/PMS system. After each cycle, the used catalyst was collected, washed with deionized water and dried for reuse. The used Fe-N@C after three cycles was also regenerated after heating at 350 °C to test its stability and reusability. PCM adsorption tests were conducted as the same procedures with the absence of PMS. All tests were conducted in duplicate.

2.4. Analysis

The mobile phase in HPLC was a mixture of methanol and UP water (55/45, v/v) with flow rate at 0.8 mL/min and 20 μL of injection volume (temperature at 35 °C), and it was detected at wavenumber of 248 nm. The intermediates of PCM were analyzed by HPLC-MS (maXis, Bruker Co., USA) to evaluate the PCM degradation pathways. The free radical species in the system were detected by an electron paramagnetic resonance (EPR) spectrometer (Bruker EMX/plus spectrometer, Germany). Electrochemical parameters of the catalysts were collected from a CHI 760D electrochemical workstation (Shanghai Chenhua Instrument Co., China). The details for the electrochemical tests as well as determination of intermediates and free radicals were given in the Supporting file.

3. Results and discussions

3.1. Characterization

The SEM images showed the intrinsic porous architecture in Fe-N@C 700 (Fig. 1a) and the SEM element mapping indicated that the N corresponded to the C distribution with Fe dispersed in the architecture (Fig. 1b). The HRTEM images showed some nanosheets decorated in the carbon layers of Fe-N@C 700 (Fig. 1c). The crystalline spacing (0.3447 nm) of nanosheets was extremely close to graphite of 0.35 nm (Fig. 1d), which indicated the form of graphite layers in the Fe-N@C 700 [23]. TEM element mapping also showed the well corresponded C, N and Fe distributions (Fig. 1e), which indicated that the intrinsic N and Fe in *Enteromorpha* biomass were co-doped in the carbon matrix after pyrolysis. ICP of the Fe-N@C 700 showed 0.60% of Fe mass, which was higher than that (0.27%) in the *Enteromorpha* biomass (Table S1). This indicated that the Fe mass was concentrated after pyrolysis.

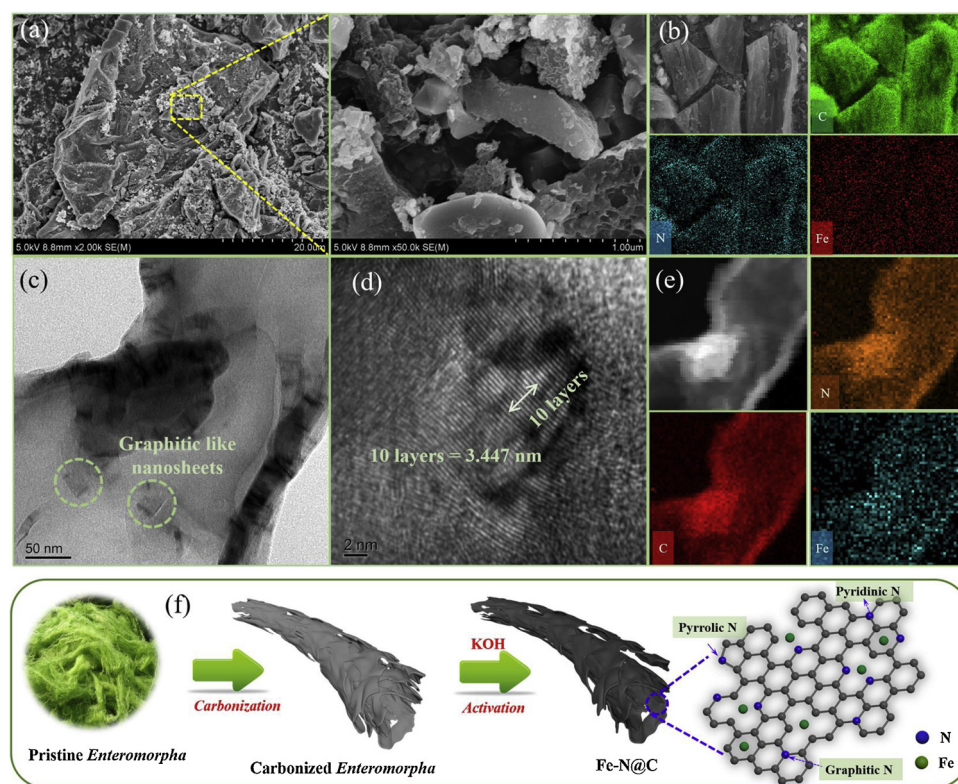


Fig. 1. (a) SEM of Fe-N@C 700 (b) SEM element mappings of Fe-N@C 700; (c) TEM of Fe-N@C 700 (50 nm); (d) TEM of Fe-N@C 700 (2 nm); (e) TEM element mappings of Fe-N@C 700; (f) preparation scheme of Fe-N@C from the *Enteromorpha* biomass.

Table 1

Surface properties of pristine *Enteromorpha* biomass, carbonized *Enteromorpha* biomass, as well as multiple Fe-N@C catalysts.

Samples	BET surface area (m ² /g)	Pore volume (cm ³ /g)	Average pore size (nm)
Pristine <i>Enteromorpha</i>	11.505	0.060	20.704
Carbonized <i>Enteromorpha</i>	24.281	0.082	13.567
Fe-N@C-600	140.405	0.244	6.941
Fe-N@C-700	638.116	0.545	3.416
Fe-N@C-800	851.654	0.692	3.249
Fe-N@C-900	983.657	0.839	3.414

Surface properties of pristine *Enteromorpha* biomass, carbonized *Enteromorpha* biomass, as well as multiple Fe-N@C catalysts were given in Table 1 and Fig. S1. The BET surface areas of *Enteromorpha* based catalysts after pyrolysis were in the range of 140.405–983.657 m²/g, extremely higher than those (11.505–24.281 m²/g) of pristine and carbonized *Enteromorpha* biomass. A richer porous architecture was created in the *Enteromorpha* based catalysts as the rise in pyrolysis temperature due to the decomposition of tar compounds in *Enteromorpha* biomass [23]. The pore volumes of these Fe-N@C catalysts were in the range of 0.244–0.839 cm³/g with average pore sizes of 3.249–6.941 nm. Such a highly porous architecture was very favorable for the adsorptive and degradative applications.

The chemical compositions of the Fe-N@C could be evaluated by the XPS measurement, which could provide the intrinsic catalytic sites for PMS activation. The total amount of N in pristine *Enteromorpha* biomass was 5.37%, and it was decreased to 3.51% after carbonization. The further decrease in the N amounts of Fe-N@C catalysts (1.93%→0.62%) were observed with the rise in pyrolysis temperature (Fig. S2), which may be ascribed to the decomposition of unstable nitrogen species at higher temperatures [35]. The three fitted peaks (398.5, 400.0 and 401.2 eV) of N 1s shown in Fig. 2a can be assigned to the pyridinic

N, pyrrolic N, and graphitic N [36,37]. It was known that the graphitic N is more thermally stable among all the nitrogen species, and it could contribute to the distortion of carbon network, which produced more defective edges for PMS activation [23,30,38,39]. An increased graphitic N fraction from atomic 28.3% (Fe-N@C 600) to atomic 50.3% (Fe-N@C 900) was observed (Fig. S3), assigning to the more transformation of pyridinic N/pyrrolic N to graphitic N with increased pyrolysis temperature. Fe 2p spectra (Fig. 2b) of these catalysts were deconvoluted, which fell in the range of Fe(III). In addition, XPS Fe 2p indicated that the atomic % of Fe (0.25–0.57%) in the *Enteromorpha* based catalysts was higher than those of pristine (0.21%) and carbonized *Enteromorpha* biomass (0.25%). This indicated that the unstable carbon was significantly decomposed with increased pyrolysis temperature, which enriched the Fe amounts in the Fe-N@C catalysts. C 1s spectrum (Fig. S4 and Table S2) of pristine *Enteromorpha* biomass could be deconvoluted into C=C (284.1 eV), C–C/C–N (285.0 eV), C–O (285.8 eV), and O–C=O (287.2 eV). In contrast, a weak π - π^* shake up satellite (290.2 eV) was observed in the C 1s spectrum of carbonized *Enteromorpha* biomass and the intensity of peak was further increased in those Fe-N@C catalysts (Fig. S5). This indicated the formation of graphitic structure at high pyrolysis temperature, which was corresponded well to their graphitic N fractions in N 1s spectra.

Raman spectra exhibited that the I_D/I_G of carbonized *Enteromorpha* was around 0.85 (Fig. S6). However, the ratios of I_D/I_G were up to 0.94–0.98 for multiple Fe-N@C catalysts after further pyrolysis at 600–900 °C. This implied that the graphitization degree of Fe-N@C was greatly improved and more defective edges were produced by the pyrolysis treatment [23,39,40]. In addition, a strong peak at 43.3° in XRD patterns was observed (Fig. S7), which can be attributed to the (100) plane of crystalline carbons in the Fe-N@C [21,41,42]. The enhanced crystalline peak implied that the graphitization degree of Fe-N@C was increased with the rise in pyrolysis temperature.

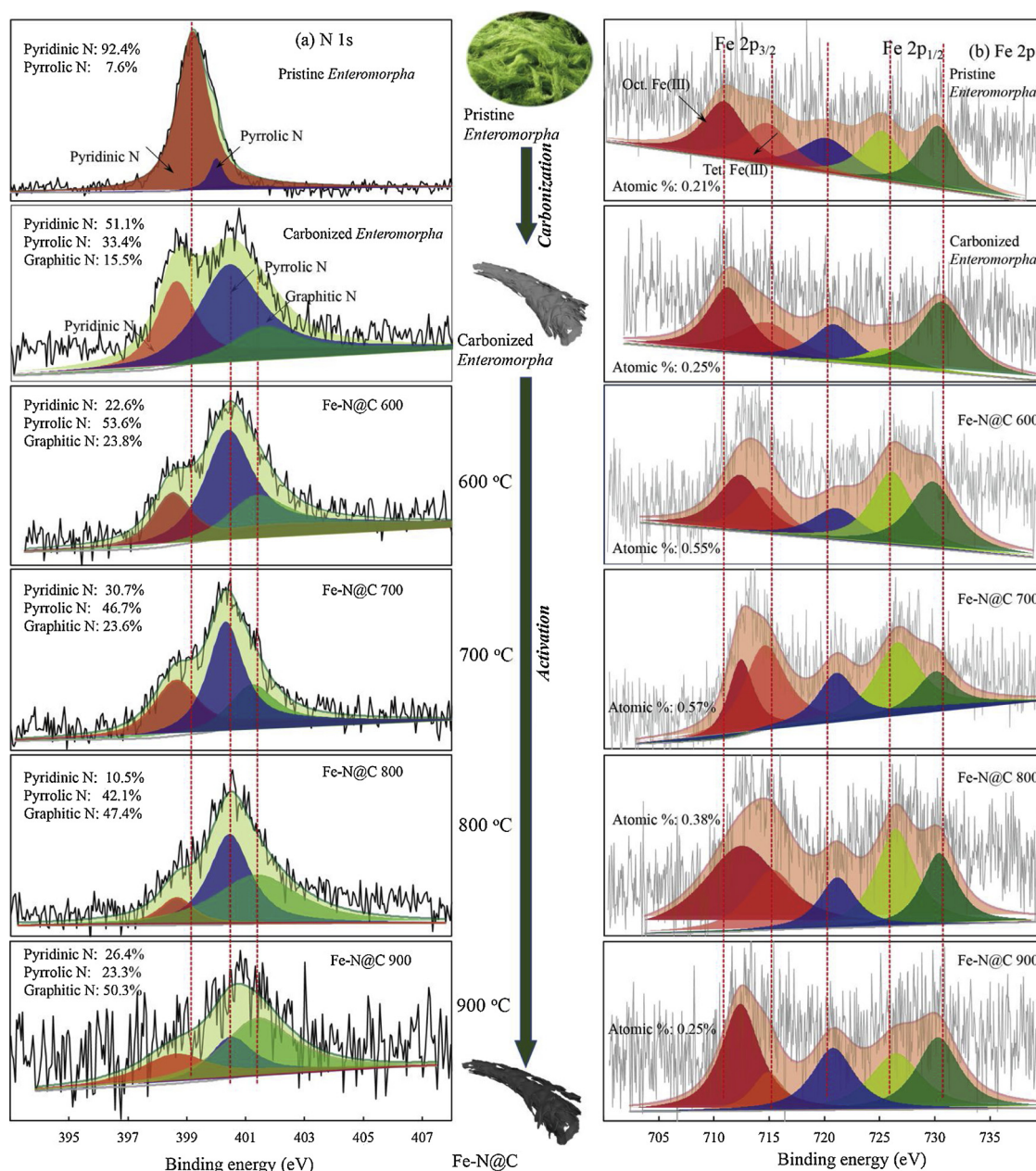


Fig. 2. XPS (a) N1 s and (b) Fe2p of pristine *Enteromorpha* biomass, carbonized *Enteromorpha* biomass, as well as multiple catalysts derived from *Enteromorpha* biomass.

3.2. PCM adsorptive and catalytic performances of multiple Fe-N@C

PCM adsorptive and catalytic capacities of Fe-N@C derived from different pyrolysis temperatures were given in Fig. 3. More than 63.2%, 64.9%, 89.5%, 89.7% of PCM could be adsorbed onto the Fe-N@C 600, 700, 800 and 900 with maximum PCM adsorption capacity (q_e , mmol/g) calculated to be 0.424, 0.430, 0.596, and 0.597 mmol/g, respectively (Fig. 3a). This indicated the considerable adsorption capacity of multiple Fe-N@C for PCM. In contrast, pristine and carbonized *Enteromorpha* biomass showed negligible PCM adsorption capacities (Fig. S8). Catalysts obtained at higher pyrolysis temperature exhibited significantly higher adsorption capacities towards PCM; this may be benefited from (i) the high surface areas of the catalysts, and (ii) the strong π - π interactions between the PCM molecules and graphitic carbon in Fe-N@C [23,39,43,44]. The removal degradation of PCM in the Fe-N@C/PMS systems were shown in Fig. 3b. Complete removal of PCM could be achieved by all Fe-N@C catalysts and the PCM removal

rate was increased from 0.0931 to 0.2472 min⁻¹ with the increase in pyrolysis temperature (Fig. S9). In contrast, the carbonized *Enteromorpha* only showed a small removal rate (0.0232 min⁻¹). The PCM removal rates showed the positive correlation ($R^2 = 0.9496$) with the fractions of graphitic N (%) in different Fe-N@C samples (Fig. 3c). This result confirmed the essential role of graphitic N for activating PMS. In addition, the removal rates also displayed a weak correlation ($R^2 = 0.8429$) with the PCM adsorption capacities by different Fe-N@C samples (Fig. 3d). This result indicated that more PCM molecules were involved in the charge-transport process as higher adsorption capacity rendered [23], which contributed to the catalytic reaction on the surface of Fe-N@C.

It was quite interesting that Fe-N@C-700 after acid treatment exhibited the better PCM removal rate (Figs. 3e and S10). The Fe atomic % in acid treated Fe-N@C-700 was only 0.14% (Fig. 3f), which showed a high Fe extraction from the pristine catalyst (0.57%). In addition, the stable graphite structure in the catalyst after acid treatment was

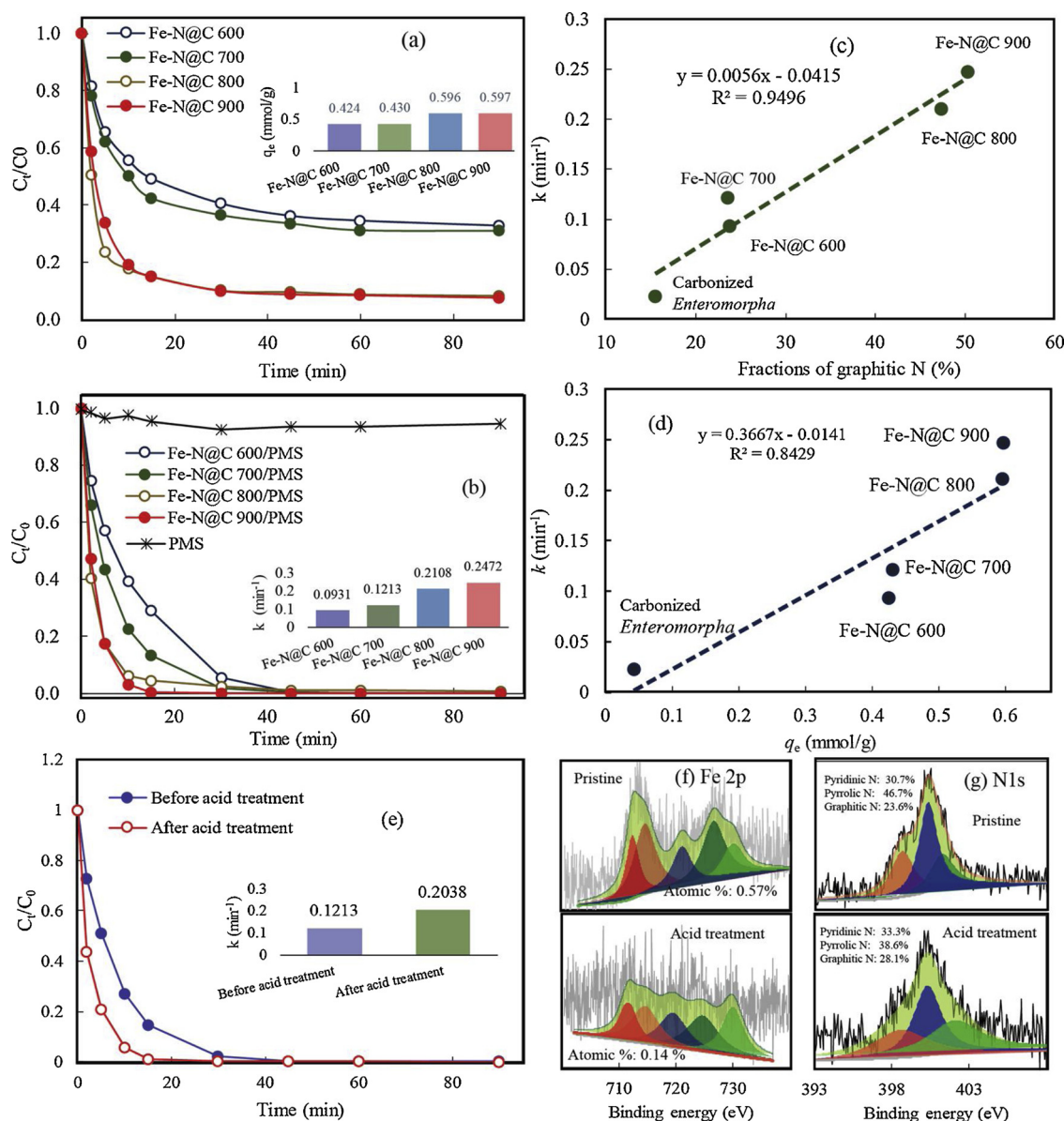


Fig. 3. PCM adsorption capacity of different *Enteromorpha* based catalysts; (b) PCM catalytic performance of different *Enteromorpha* based catalysts; (c) The correlation between PCM removal rate and graphitic N (%) fractions in different *Enteromorpha* based catalysts; (d) The correlation between PCM removal rate and adsorption capacity achieved by different *Enteromorpha* based catalysts; (e) PCM catalytic performance of Fe-N/C-700 before and after acid treatment; (f) N 1s and (g) Fe 2p of Fe-N/C 700 before and after acid treatment ([PMS]₀ = 0.5 mM, [PCM]₀ = 10 mg/L, catalyst dose = 0.1 g/L, pH = 5.6).

observed (Fig. 3g). This indicated that the Fe species in the catalyst did not contribute to the catalytic reaction, and the superior removal efficiency after acid treatment might be probably due to the forms of new active sites after Fe extraction [22]. This was also confirmed by the increased adsorption capacity of Fe-N/C-700 after acid treatment, which induced more porous structures for PCM adsorption (Fig. S11).

3.3. PCM degradation by other biomass-based catalysts

Other N rich biomass (soybean, *spirulina*, bean stalk, and kelp) were also employed for preparing the metal-free catalysts based on the same procedures. Adsorptive and catalytic performances of these biomass-based catalysts for PCM were presented in Figs. 4 and S12. The PCM adsorption onto these catalysts varied from 30.3 to 99.8% with BET surface areas in the ranges of 183.960–727.271 m²/g (Fig. S13 and Table S3). The high BET surface area (727.271 m²/g) of Soybean based catalyst only show a small adsorption capacity (30%) towards PCM. As a result, the higher surface areas did not correspond to the superior

adsorptive performance, which indicated that other forces, e.g. chemisorption, electrostatic attraction, and π - π interactions, also contributed to the PCM adsorption [23]. The PCM removal rates (k min⁻¹) of *Enteromorpha*, soybean, *Spirulina*, bean stalk, and kelp derived catalysts were calculated to be 0.1213, 0.0106, 0.032, 0.0319 and 0.2952 min⁻¹, which showed a weak correlation ($R^2 = 0.8603$) with their PCM adsorption capacities (Figs. S14 and 4b). XPS spectra of these biomass-based catalysts were shown in Figs. S15 and 4c. The atomic N of these catalysts were in the range of 1.45–7.03%. The high N content (7.03%) in the *spirulina*-based catalyst only exhibited a small PCM removal rate (0.032 min⁻¹). As a result, the high N contents in the catalysts did not mean the high catalytic performance. Different fractions of pyridinic N, pyrrolic N, and graphitic N were also deconvoluted from the XPS N 1s of these catalysts (Fig. 4c). The kelp showed an extremely high graphitic N fraction (57.3%), which corresponded to the high removal rate (0.2952 min⁻¹). Most importantly, a highly positive correlation ($R^2 = 0.987$) was observed between the removal rates k and the graphitic N (%) compositions in these biomass-based catalysts (Figs. 4d

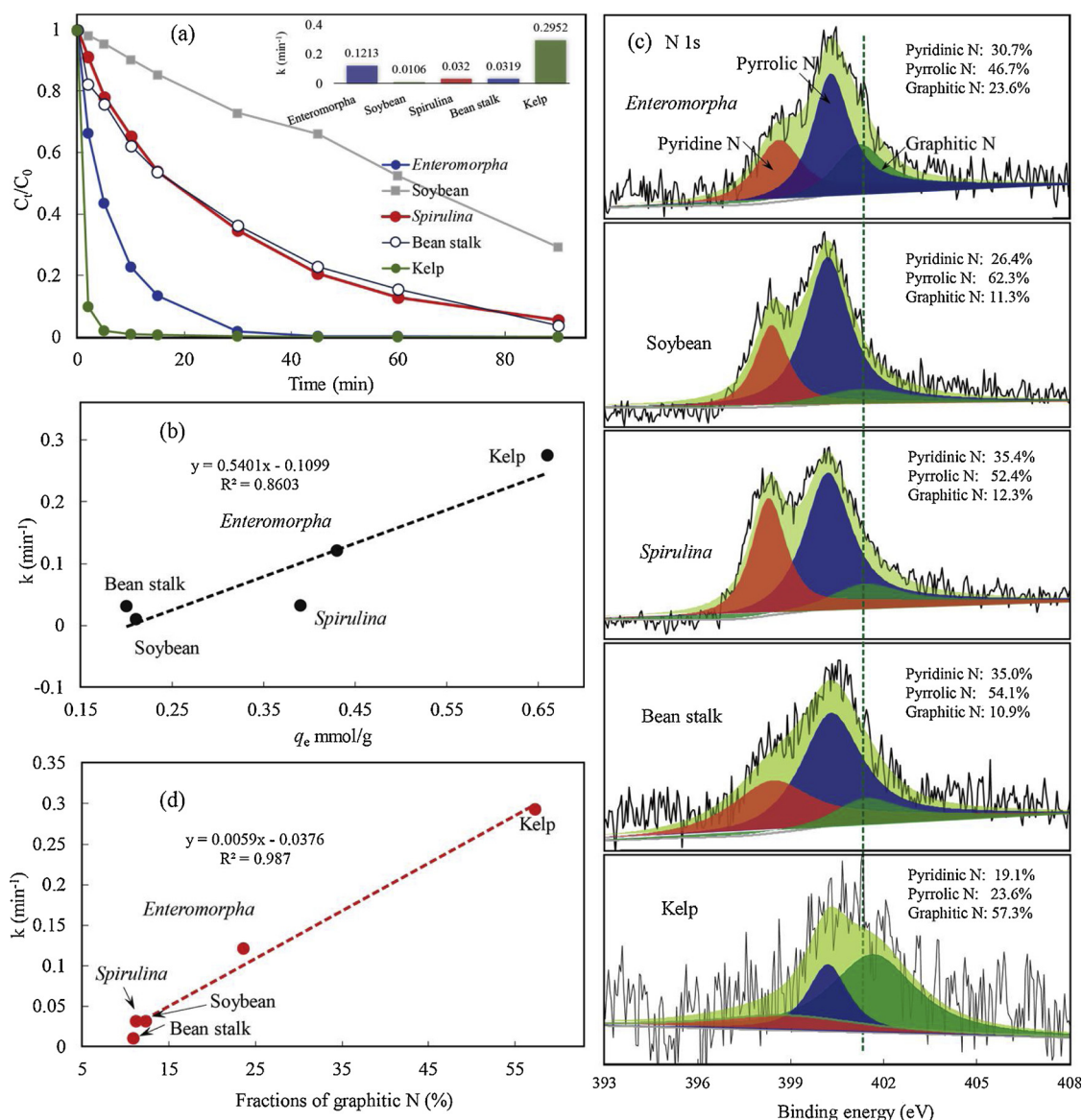


Fig. 4. (a) PCM catalytic performance of multiple biomass-based catalysts; (b) The correlation between PCM removal rate and adsorption capacity achieved by multiple biomass-based catalysts; (c) N 1s of multiple biomass-based catalysts; (d) A correlation between PCM removal rate and fractions of graphitic N (%) in different biomass-based catalysts; ([PMS]₀ = 0.5 mM, [PCM]₀ = 10 mg/L, catalyst dose = 0.1 g/L, pH = 5.6).

and S16). These results further confirmed that the graphitic N compositions dominated the PCM catalytic reaction.

3.4. PCM degradation in different conditions

PCM catalytic performances in different operation conditions were conducted to evaluate the parameters required in practical use. Effect of Fe-N@C dosage on PCM degradation was shown in Fig. 5a. In a low Fe-N@C dosage (0.02 g/L), 80% of PCM (k at 0.0173 min⁻¹) could be removed within 90 min and only 10% of adsorption was involved (Figs. S18 and S19a). As the dosage increased to 0.1 g/L, PCM could be completely removed within 30 min (k : 0.1224 min⁻¹) and the adsorption of PCM onto Fe-N@C was increased to 60%. As a result, a high Fe-N@C dosage both contributed to the improved catalytic and adsorptive performances due to the increase in the active sites.

PCM removal rates at different PMS dosages were given in Fig. 5b. The removal rate k was only 0.0654 min⁻¹ at PMS loading of 0.25 mM, and it was significantly increased to 0.1213 min⁻¹ at PMS loading of 0.5 mM (Fig. S19b). A further increase in PMS loading from 0.5 to

1.0 mM only resulted in a slight rise in k from 0.1213 to 0.1306 min⁻¹. The increasing PMS dosage would activate more sites on the surfaces of Fe-N@C to attack PCM molecules. As a result, PMS dosage was the rate limiting factor for PCM degradation at low PMS dosage [45]. However, the active sites were gradually saturated at high PMS loadings, which means that the amounts of active sites on the surfaces of catalyst was the key constraint factor at high level of PMS [45].

PCM degradation in terms of pH was shown in Fig. 5c. Interestingly, PCM removal rate increased at more acidic or alkaline conditions. It was observed that PCM adsorption was greatly enhanced with the decrease of pH, partially due to the positively charged surface of Fe-N@C at lower pH conditions (Fig. 5d). As a result, the charge-transport process was accelerated and thus the increase in catalytic performances were observed [19]. Miao suggested that the ¹O₂ generated at acidic condition through Eq. (1) can also lead to the better catalytic activity [46]. As for the alkaline condition, PMS activation in alkaline conditions could be facilitated because excessive OH⁻ in solution was favorable to donate an electron as compared with the H₂O molecules [47]. Although the adsorptive performance at pH = 10.5 was relatively

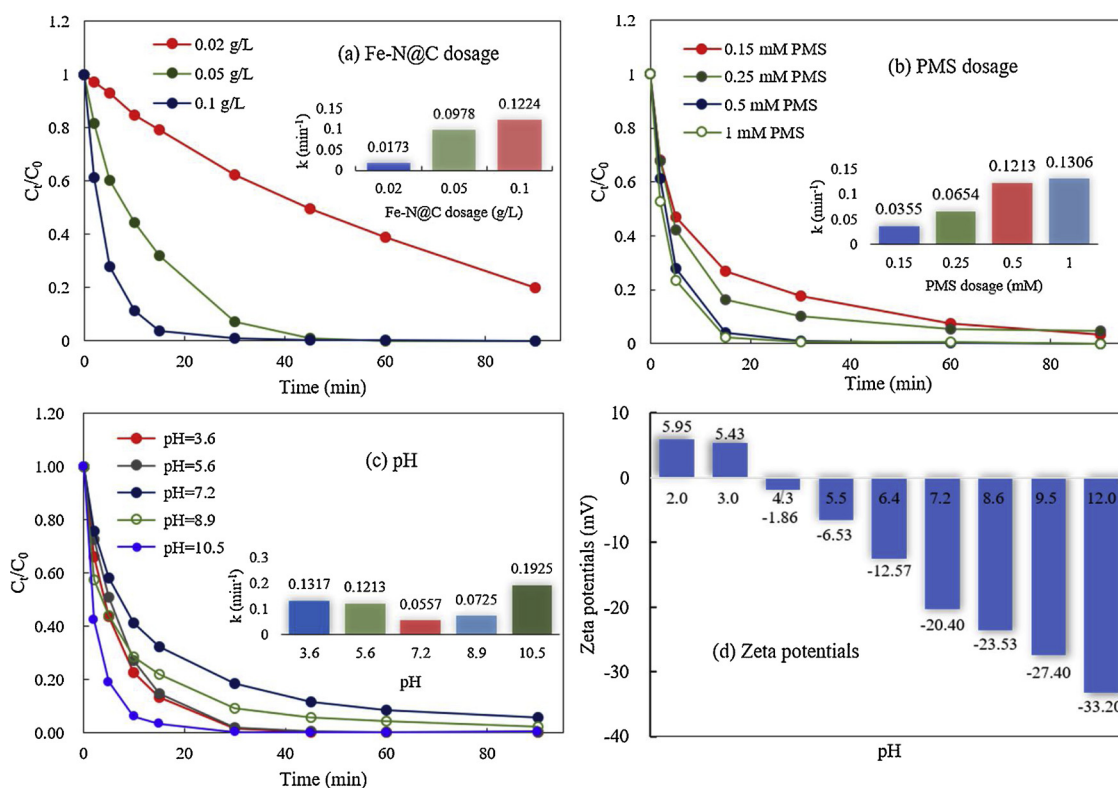
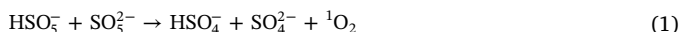


Fig. 5. PCM degradation in different conditions (a) Fe-N@C dosage; (b) PMS dosage; (c) pH; (d) zeta potentials of Fe-N@C in terms of pH ([PMS]₀ = 0.5 mM, [PCM]₀ = 10 mg/L, Fe-N@C dose = 0.1 g/L, pH = 5.6).

poor (Fig. S20), an enhanced catalytic performance also occurred, which was attributed to more reactive radicals generated during PMS activation at alkaline condition [48,49].



3.5. Radical and non-radical pathways

Since PMS activation can occur through both the radical and non-radical oxidation, the radicals generated in Fe-N@C/PMS system should be intensively identified [15,28,50]. Herein, different radical quenching reactions based on the radical scavengers (EtOH, TBA, *p*-BQ and *L*-histidine) was conducted. EtOH is the effective scavenger for both $\text{SO}_4^{\cdot-}$ and $\cdot\text{OH}$ radicals (reaction rate of $k_{\text{SO}_4^{\cdot-} + \text{EtOH}} = 1.6 \times 10^7 \text{ M}^{-1} \text{ s}^{-1}$ and $k_{\text{OH} + \text{EtOH}} = 1.9 \times 10^9 \text{ M}^{-1} \text{ s}^{-1}$). In contrast, TBA is the typical quenching agent for $\cdot\text{OH}$ ($k_{\text{OH} + \text{TBA}} = 6.0 \times 10^8 \text{ M}^{-1} \text{ s}^{-1}$). The existence of high levels of EtOH and TBA showed the very limited inhibition effects on PCM degradation and still 100% of degradation efficiency was retained within 90 min with only a small decrease in removal rate k (Fig. 6a and b). This implied that the radical pathways involving $\text{SO}_4^{\cdot-}$ and $\cdot\text{OH}$ were indeed generated in the Fe-N@C/PMS system but only donated a very small contribution to the PCM removal.

Furthermore, the superoxide anion radical ($\text{O}_2^{\cdot-}$) was determined by using *p*-BQ as scavenging reagent ($1.0 \times 10^9 \text{ M}^{-1} \text{ s}^{-1}$). It is found that 80% of efficiency (k : 0.0266 min^{-1}) was retained with adding 5 mM of *p*-BQ and the removal efficiency was further decreased to only 37% (k : 0.012 min^{-1}) at 25 mM of *p*-BQ (Figs. 6c and S21c). This indicated that the radical pathway of $\text{O}_2^{\cdot-}$ was quite important in the PCM degradation reaction. The *L*-histidine was a unique scavenger for ${}^1\text{O}_2$ and the adding of *L*-histidine into the system caused a significant inhibitory effect on PCM removal, with only 30% of removal efficiency (k of 0.0094 min^{-1}) retained within 90 min at the addition of 25 mM *L*-histidine (Figs. 6d and S21d). This suggested that non-radical pathway (${}^1\text{O}_2$) was also predominant in the Fe-N@C/PMS system.

EPR spectra in Fe-N@C/PMS system using DMPO for trapping $\text{O}_2^{\cdot-}$ and TEMP for ${}^1\text{O}_2$ were shown in Fig. 6e and f. No signals of $\text{O}_2^{\cdot-}$ and ${}^1\text{O}_2$ are detected for sole PMS. However, characteristic signals of DMPO- $\text{O}_2^{\cdot-}$ appeared in the PMS/Fe-N@C and PMS/Fe-N@C/PCM systems; this indicated that the Fe-N@C greatly promoted the PMS activation for $\text{O}_2^{\cdot-}$ generation. Similarly, the strong signals of triplet EPR spectra with equal intensities corresponding to the oxidation of TEMP by ${}^1\text{O}_2$ were detected in PMS/Fe-N@C and PMS/Fe-N@C/PCM systems. As a result, a large amount of ${}^1\text{O}_2$ was also produced in the Fe-N@C/PMS system for PCM degradation.

To further confirm the presence of ${}^1\text{O}_2$, PCM degradation tests in different solvents were conducted. By exchanging the solvent from H_2O to D_2O , the lifetime of ${}^1\text{O}_2$ exists in the solution will be extended more than 10 times [51]. Aiming at distinguishing the role of ${}^1\text{O}_2$, the PCM concentration in both H_2O and D_2O solution was added up to 40 mg/L while other conditions remained constant. As shown in Fig. S22(a), only 79.3% of PCM (40 mg/L) was removed (k : 0.0281 min^{-1}) within 90 min in H_2O solution, whereas the degradation efficiency within 90 min in D_2O solution was 99.2% (k : 0.0495 min^{-1}). It can be concluded that singlet oxygen was truly generated during the degradation process, and the longer lifetime of ${}^1\text{O}_2$ triggered better removal efficiency. This is further endorsed by the result of EPR spectra (Fig. S22(b)), in which the intensity of TEMP adducts signal in Fe-N@C/PMS/ H_2O system is much weaker than that in Fe-N@C/PMS/ D_2O system.

The formation of $\text{O}_2^{\cdot-}$ may attribute to the activation of PMS by Fe-N@C catalyst, in which electron transfer plays an important role. Hydroxyl radical, which emerged during the PMS activation process, reacted with hydrogen peroxide in the Fe-N@C/PMS system to generate perhydroxyl radicals. Then, perhydroxyl radicals decomposed and gave rise to the superoxide anion radical (Eqs. (2)–(8)) [48,49,52,53].



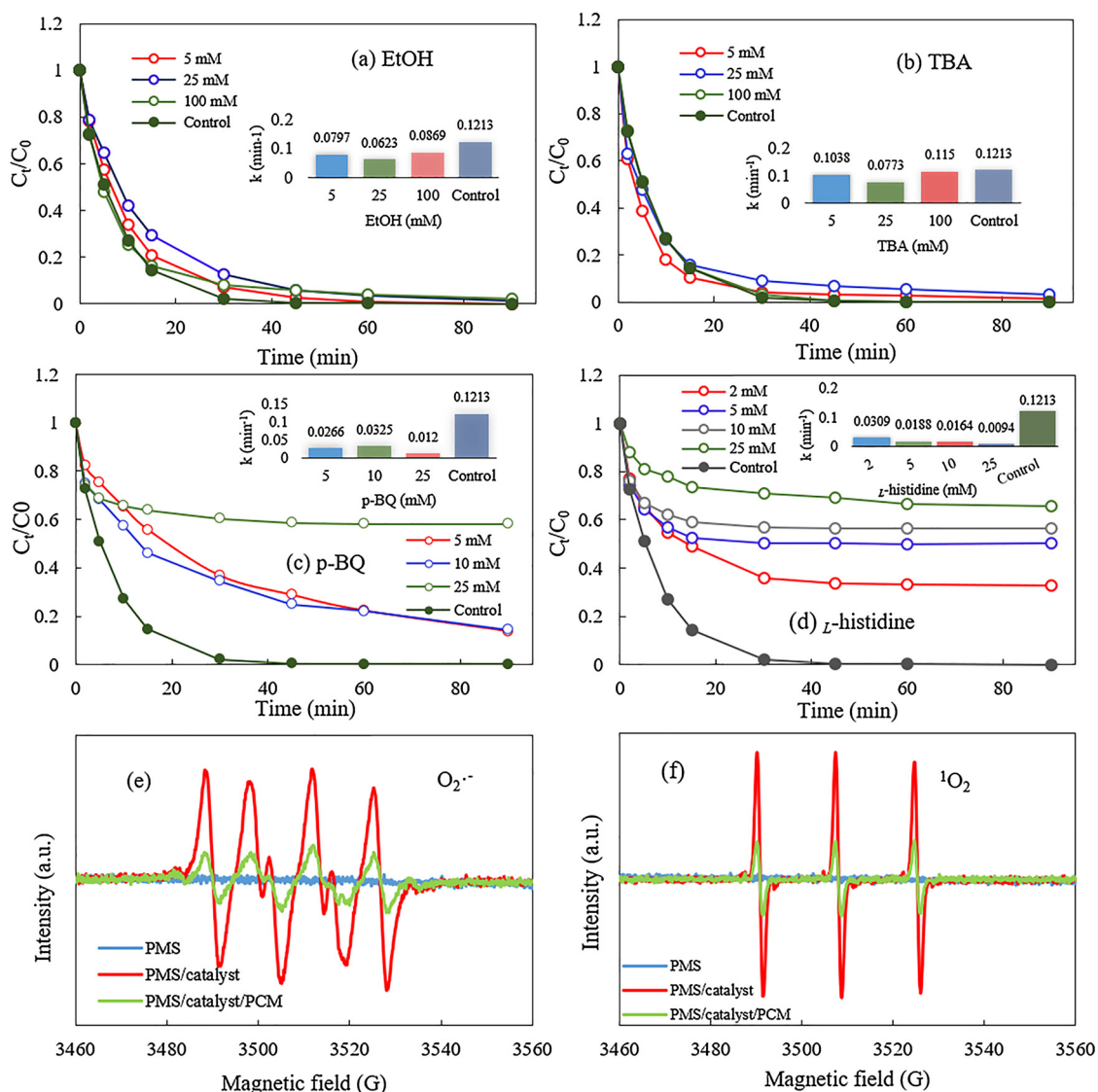
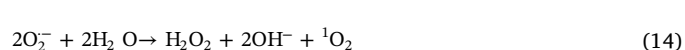


Fig. 6. PCM degradation in different scavenger systems (a) EtOH, (b) TBA, (c) BQ, (d) *L*-histidine; (e) ESR spectra in Fe-N@C/PMS system using DMPO for $O_2^{\cdot-}$; (f) TEMP for 1O_2 ; ([PMS]₀ = 0.5 mM, [PCM]₀ = 10 mg/L, Fe-N@C dose = 0.1 g/L).



Typically, the electron-rich ketonic groups (C=O) located on the boundaries of sp^2 -conjugated carbon lattice play a significant role in interacting with PMS through nucleophilic addition and mediating dioxirane intermediates to generate singlet oxygen [54,55]. The carbonyl groups distributed on the surface of Fe-N@C might be the active centers for the evolution of 1O_2 . Shao proposed an electron conduction mechanism between PMS (electron donor) and electrophilic C=O groups (electron acceptor) [56]. PMS anion radicals ($SO_5^{\cdot-}$), which are generated by releasing an electron from PMS, will be further combined to form $S_2O_8^{2-}$ or SO_4^{2-} ions, and meanwhile produce 1O_2 (Eqs. (9)–(11)). Moreover, $O_2^{\cdot-}$ also acts a pivotal role in the generation of 1O_2 . For instance, singlet oxygen could be produced by the reaction of superoxide anion radical and hydroxyl radical (or perhydroxyl radical) (Eqs. (12)–(15)).



The electrochemical evaluation was conducted to further investigate the charge transfer between PMS molecule and Fe-N@C catalyst. As displayed in Fig. 7a, the increased current in the catalyst/PMS and catalyst/PMS/PCM systems was observed as compared with that of sole catalyst during linear sweep voltammetry (LSV) detection. This suggested that the addition of PMS could interact with the active sites of Fe-N@C, forming the metastable reactive complex [23]. Fitting of Nyquist plots represented the charge-transfer resistance value (120.3 Ω) of Fe-N@C (Fig. S23), which showed the excellent conductivity and electron-transfer property of Fe-N@C. In addition, current outputs at

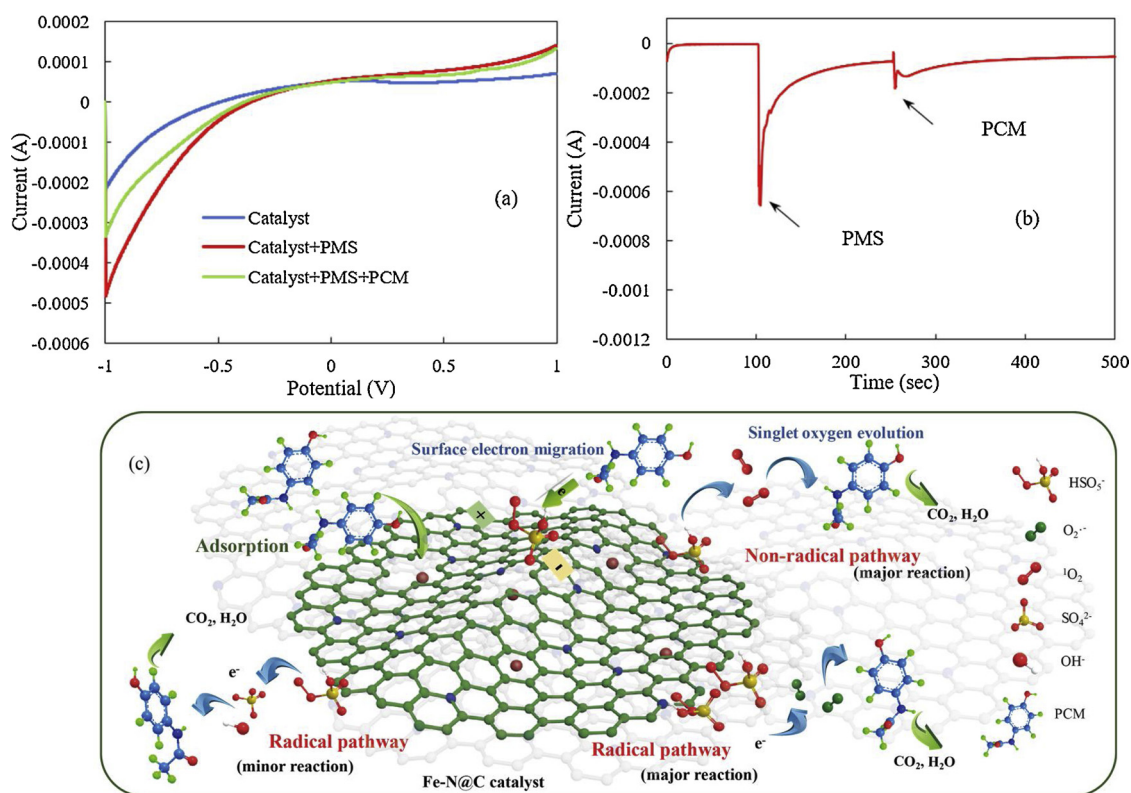


Fig. 7. (a) LSV curves under different conditions; (b) i-t curve of Fe-N@C ([PMS]₀ = 1 mM; [PCM]⁰ = 10 mg/L, pH_i = 7.0); (c) Mechanism scheme of PCM removal in Fe-N@C/PMS system.

the Fe-N@C coated electrode after PMS addition followed by PCM addition were given in Fig. 7b. The significant current generations with the adding of PMS (1 mM) at 100 s and PCM (10 mg/L) at 250 s was observed. This was an evidence proving that the strong electron transfer occurred among the PMS, PCM molecules and the surface of catalyst [57,58].

Based on all mentioned above, it can be concluded that both the radical pathways of $\text{O}_2^{\cdot-}$ and non-radical $^1\text{O}_2$ activated in the Fe-N@C/PMS system were the primary mechanisms for the PCM degradation, while the radicals $\text{SO}_4^{\cdot-}$ and OH^{\cdot} only showed a limited contribution in Fe-N@C/PMS system. Besides, the electron transfer among the PMS, PCM molecules and the surface of catalyst played an essential role in the degradation of PCM. Both singlet oxygen and surface electron migration mechanisms occurred with a coupled system as the non-radical pathways (Fig. 7c).

3.6. DFT calculations for the electronic properties of catalysts

DFT calculations were further conducted for the insights into the reaction sites on the Fe-N@C for PMS activation. It was known that the negative and positive regions in the electrostatic potentials (ESP) map represented the active sites for reduction and oxidation reactions [59]. Considering the essential role of graphitic N in the catalytic reaction, the ESP distributions on the graphitic N atom doped graphene fragments before and after PMS being adsorbed were investigated (Fe was not considered because of its absence in catalytic reaction). Fig. 8a shows an optimized pure graphene without the graphitic N, in which the ESP is evenly distributed on each C atom. After introducing the graphitic N on the surface of the graphene fragment, the ESP distribution becomes uneven (Fig. 8b). The positive potential is mainly located around the graphitic N atom while other atoms were not significantly affected. This result indicated that the homogeneous carbon network was greatly disturbed with endowed high chemical potentials. Free PMS molecule given in Fig. 8c showed a very negative potential

around its atoms. The possible adsorption model of PMS molecule onto graphitic N atom was shown in Fig. 8d. The ESP map suggested that the most electronegative part of the PMS being adsorbed onto the catalyst fragment was the area around the graphitic N atom and PMS molecule. The adsorption energies (ΔE_{ads}) of PMS molecular adsorbed onto the graphitic N area was calculated to be -2.62 eV. The extremely high ΔE_{ads} indicated the graphitic N exerted the strong binding affinity towards the PMS molecules, which was beneficial to promote the PMS activation and nonradical oxidation on surface of the catalysts [43]. As above, it can be concluded that the doped graphitic N atom is the catalytic site of Fe-N@C for PCM degradation.

3.7. Effect of anions and humic acid on PCM degradation

PCM degradation with respect to different anions (H_2PO_4^- , Cl^- and HCO_3^-) in Fe-N@C/PMS system was shown in Fig. 9. It was reported that the H_2PO_4^- always exhibited the robust affinity with the active sites of catalysts, which competitively inhibited the PMS activation [60,61]. However, H_2PO_4^- with the backgrounds of 2–10 mM showed a marginal effect on the PCM degradation (Figs. 9a and S24a), which indicated that the PCM degradation in Fe-N@C/PMS system was most probably a nonradical process dominated by $^1\text{O}_2$ [38]. PCM degradation by Fe-N@C/PMS at different Cl^- levels was presented in Fig. 9b. The addition of 2 mM chloride only resulted in a small decrease in the removal rate from 0.1213 to 0.0946 min⁻¹. The chloride could consume the $\text{SO}_4^{\cdot-}$ or OH^{\cdot} radicals, forming Cl^{\cdot} and $\text{Cl}_2^{\cdot-}$ radicals with lower redox potentials (Eqs. (16)–(19)). However, as the chloride levels were further increased to 10 mM, a distinct increase in the k (0.1493 min⁻¹) was observed, which was even higher than that (0.1213 min⁻¹) in the absence of Cl^- . In addition to be the radical scavengers, excessive Cl^- with negative charge could also donate electrons to PMS, generating superabundant active chlorine species and sulfate radicals under the activation of Fe-N@C [47], which could participate in the PCM degradation process [42]. PCM degradation in the background of different

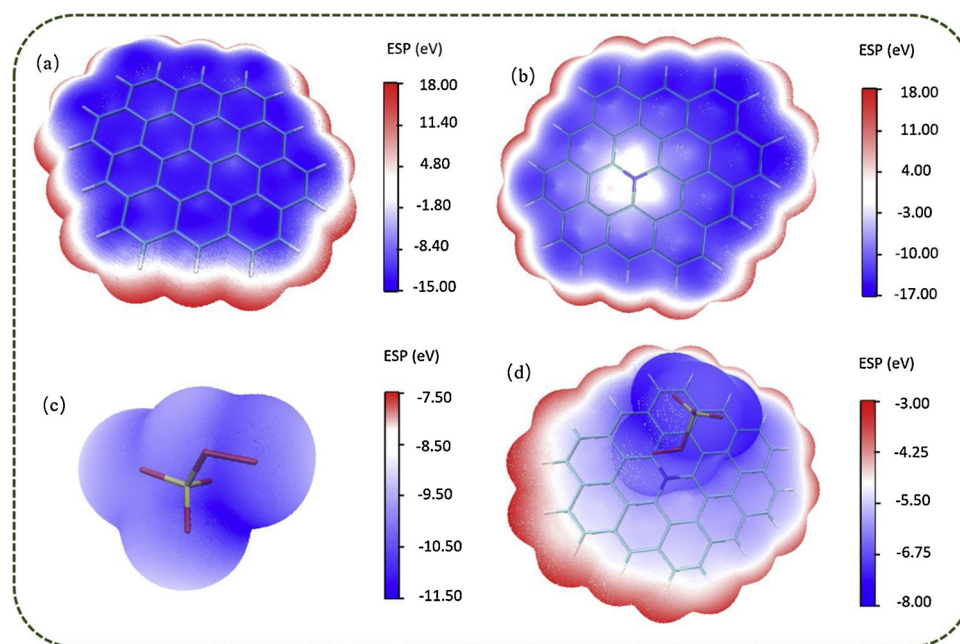


Fig. 8. Distributions of electrostatic potential (ESP) for different graphene fragments via DFT calculations: (a) pure graphene, (b) graphene with doping graphitic N atom, (c) PMS molecule, and (d) graphene with PMS be adsorbing.

levels of HCO_3^- showed the similar phenomenon (Fig. 9c), which was also in accordance with other reported works [42].



Unlike anions such as H_2PO_4^- , Cl^- and HCO_3^- , a stronger inhibitory effect was observed in the background of HA (2 mM) and the removal rates was decreased from 0.1213 to 0.0397 min^{-1} (Fig. 9d). Interestingly, a further increase in HA from 2 to 10 mM only resulted in a slight k decrease from 0.0397 to 0.0323 min^{-1} , which was also existed

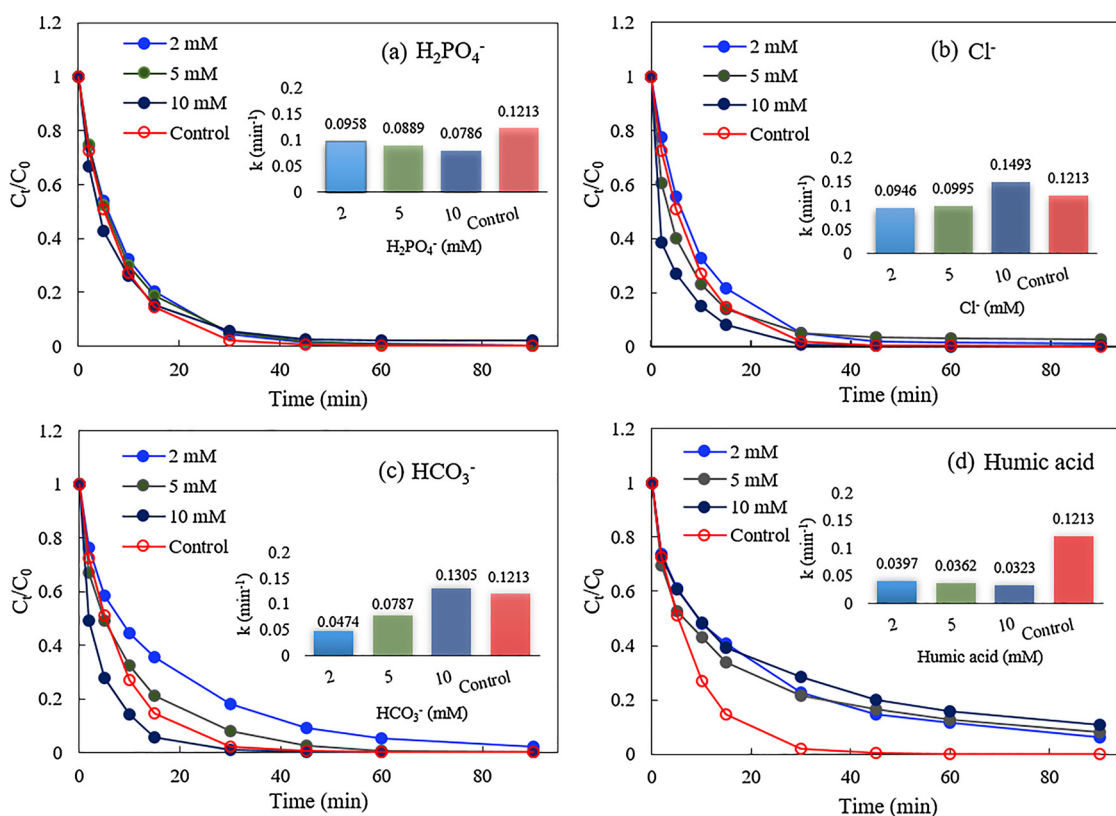


Fig. 9. Effect of different anions and humic acid on PCM degradation (a) H_2PO_4^- ; (b) Cl^- ; (c) HCO_3^- ; (d) Humic acid ($[\text{PMS}]_0 = 0.5 \text{ mM}$, $[\text{PCM}]_0 = 10 \text{ mg/L}$, Fe-N@C dose = 0.1 g/L).

in other reported works [42,62–64]. Luo suggested the existence of weak reactive activity between $^1\text{O}_2$ and HA [42], which resulted in a small decrease in the non-radical reaction in Fe-N@C/PMS system. In addition, HA would be adhered on the surface of catalysts, covering the catalytic sites and preventing the interaction between the catalysts and PMS [62,65]. Nevertheless, HA might also have the stimulant effect. It is widely accepted that hydroquinones, quinones and phenols in HA could generate semiquinone radicals, which own the ability to activate PMS producing $\text{SO}_4^{\cdot-}$ and $^{\cdot}\text{OH}$ [62–66]. Besides, the quinone group ($\text{C}=\text{O}$) content in HA could appreciably stimulate the self-decomposition of PMS and facilitate the formation of $^1\text{O}_2$, thus enhancing the degradation of PCM in some degrees [55]. Therefore, part of retardation effect might be counteracted by the stimulant effect and finally achieve a balance.

Basically, the high removal rates of PCM achieved at high levels of coexisting anions and humic acid also contributed to the radical and non-radical mechanisms in the Fe-N@C/PMS systems.

3.8. Reusability and stability of catalyst

To test the stability and reusability of Fe-N@C for PMS activation, catalytic performances of the catalyst during the consecutive runs were performed at the same catalytic conditions. Fig. 10 showed that complete degradation of PCM still could be achieved after three cycles with the k decreasing from 0.1213 to 0.0556 min^{-1} , which demonstrated the excellent stability and reusability for PMS activation. The non-negligible decrease in removal rate may be caused by the coverage of surface sites by the adsorbed PCM as well as intermediates of PCM, which would reduce the contact area of Fe-N@C with PMS, thus contributing to the reduction in the catalytic activity. Compared with the fresh Fe-

N@C, crystalline spacing (0.3316 nm) of nanosheets in used Fe-N@C were also observed (Fig. 10b). In addition, the fractions of π - π^* shake up satellite C (Fig. 10c) and graphitic N (Fig. 10d) in used catalyst were almost the same as those in fresh sample, implying that the structure of catalyst was stable after three successive cycles. The Fe 2p of used Fe-N@C only showed a small fraction change from Tet. Fe(III) to Oct. Fe(III) as compared with that of pristine catalyst (Fig. 10e). The PCM removal rate of used Fe-N@C was mostly recovered (k : 0.1142 min^{-1}) after heat regeneration (350 $^{\circ}\text{C}$). The adsorbed PCM and intermediates could be removed from the surface of Fe-N@C after calcination, and therefore, the catalytic activity of used catalyst could be mostly recovered.

3.9. Degradation pathways analysis

The theoretical calculations were then used to further understand the PCM degradation in Fe-N@C/PMS system [67]. Fukui function is a promising access to predict the susceptibility of PCM molecule attacked by different radicals [68–70]. The optimized PCM model was presented in Fig. 11a. The Fukui function values of f^+ and f^- (for the predicting the molecular reactivity to radical attack by $\text{O}_2^{\cdot-}$ and electrophilic attack by $^1\text{O}_2$) were presented in Table 2 and their contour surfaces were shown in Fig. 11b and c. The highest f_0 values of PCM were around the C2-C6 atoms in benzene ring, which indicated that the benzene ring was the most susceptible to be attacked by radical $\text{O}_2^{\cdot-}$. In contrast, the high f_{A} values were located at 11O, 1C, 10O, 4C and 7N atoms, which indicated the high activities of 1C-11O, 8C-10O and 4C-7N to be attacked by $^1\text{O}_2$. In addition, other C atoms (2C, 3C, 5C and 6C) in benzene ring also showed high potential to be attacked by $^1\text{O}_2$ for the cleavage of benzene ring. As a result, the different pathways for PCM

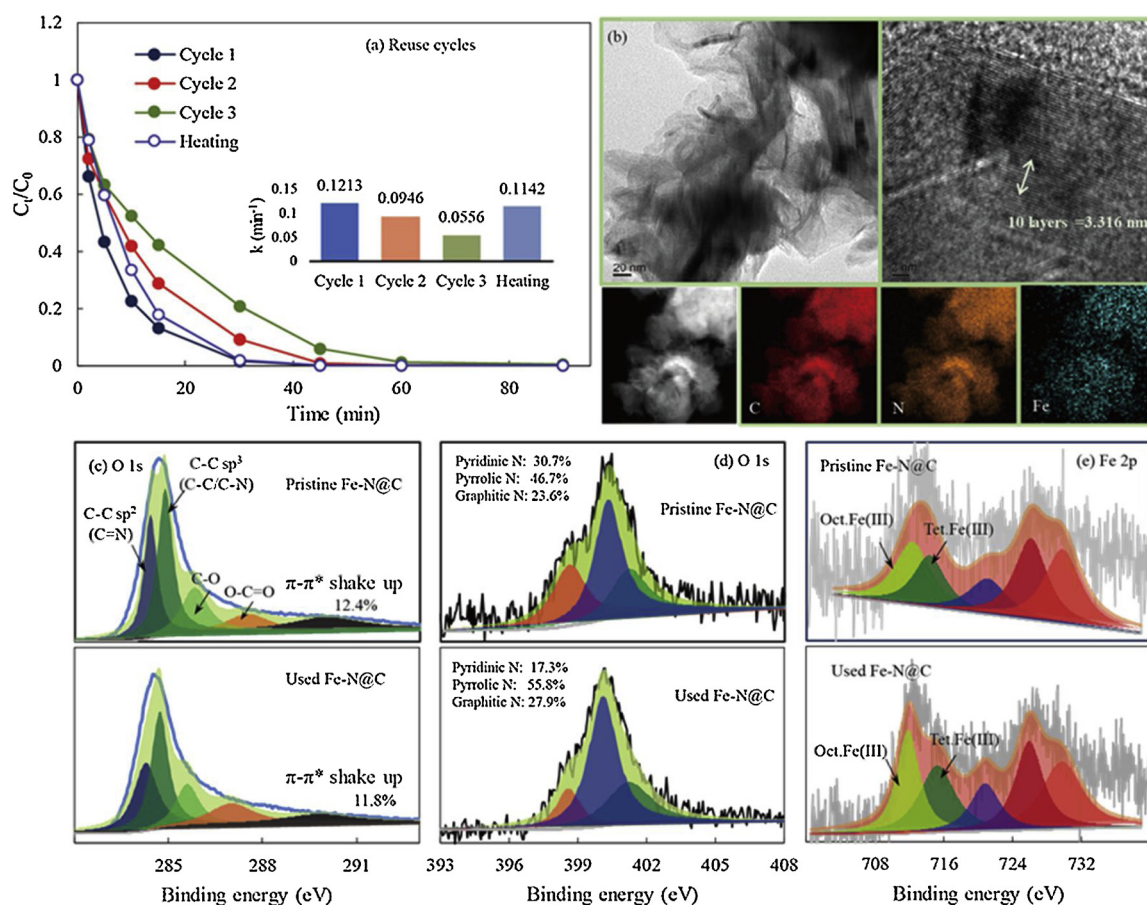


Fig. 10. Reuse cycles of Fe-N@C 700 for PCM; (b) TEM as well as elemental mappings of used Fe-N@C 700; (c) O 1s; (d) N 1s; (e) Fe 2p of fresh Fe-N@C and used Fe-N@C.

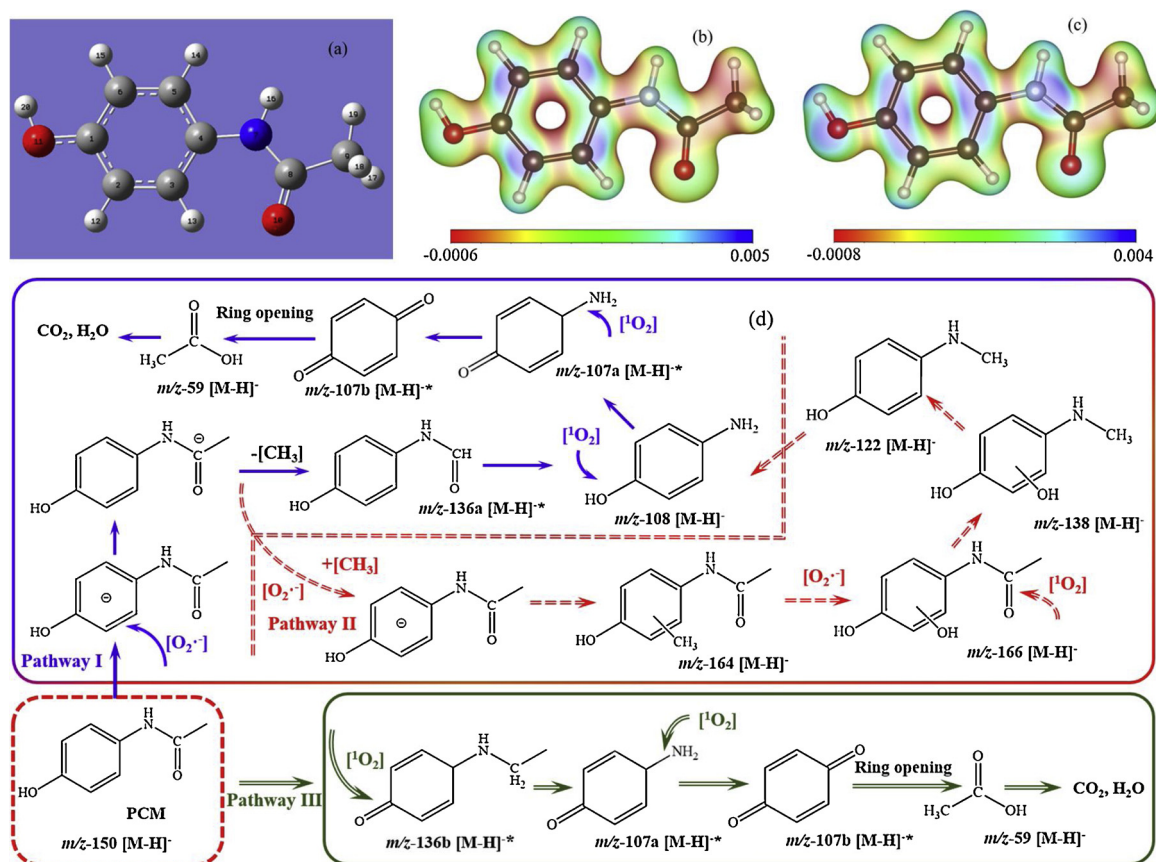


Fig. 11. (a) Optimized structure of PCM and the numbering system (gray: carbon; red: oxygen; blue: nitrogen; white: hydrogen); (b) contour surfaces of Fukui function values of f^+ for radical attack, (c) Fukui function values of f^- for electrophilic attack; and (d) potential degradation pathways of PCM in Fe-N@C/PMS system (* hypothetical intermediate) (For interpretation of the references to colour in this figure legend, the reader is referred to the web version of this article).

Table 2
The f^+ and f^- in PCM molecule.

Atom	f^+	f^-	Atom	f^+	f^-
1C	0.064	0.083	12H	0.050	0.039
2C	0.093	0.065	13H	0.039	0.029
3C	0.083	0.055	14H	0.049	0.038
4C	0.063	0.078	15H	0.050	0.039
5C	0.091	0.065	16H	0.025	0.033
6C	0.091	0.063	17H	0.021	0.023
7N	0.039	0.075	18H	0.021	0.023
8C	0.030	0.035	19H	0.014	0.015
9C	0.016	0.017	20H	0.034	0.040
10O	0.056	0.079	Total	1.000	1.000
11O	0.072	0.105			

degradation might be involved considering the radical attack ($O_2^{\cdot-}$) and electrophilic attack (1O_2).

HPLC-MS analyses (negative model) were also carried out to identify the degradation intermediates of PCM in Fe-N@C/PMS system after 0, 5 and 15 min of irradiation. The degradation intermediates were presented in Table S6 and Fig. S26. Basically, three degradation pathways were denoted according to the degradation intermediates and DFT calculations. (i) In the pathway I, the radical $O_2^{\cdot-}$ attacked the susceptible benzene ring of PCM and injected free radical electrons into the benzene ring. An extended pi bond was formed due to the connection of the N-lone pair electron with C = O bond and benzene ring. As a result, the free radical electron was transferred to the acylamino group and then led to demethylation on the acylamino group, forming the intermediate of p-hydroxyformanilide $m/z-136a$ [M-H] $^-$. It was followed by a deacylation reaction, forming the intermediate of aminophenol

($m/z-108$ [M-H] $^-$) [6]. The intermediates of p-aminobenzoquinone ($m/z-107a$ [M-H] $^-$) and p-benzoquinone ($m/z-107b$ [M-H] $^-$) could be transformed from the p-aminophenol ($m/z-108$ [M-H] $^-$) as the strong attack of 1O_2 to the 4C-7 N bond. It was further degraded into the carboxylic acids after the ring cleavage [71,72]. These carboxylic acids could be converted into CO_2 and H_2O which finally realized the mineralization of PCM molecules. (ii) In the pathway II, the PCM degradation started with the methylation on the susceptible benzene ring and subsequent hydroxylation due to the attack of radical $O_2^{\cdot-}$ [73], forming the intermediates with $m/z-164$ [M-H] $^-$ and $m/z-166$ [M-H] $^-$. After the further deacylation ($m/z-138$ [M-H] $^-$), dihydroxylation ($m/z-122$ [M-H] $^-$) and demethylation reactions [74], the p-aminophenol ($m/z-108$ [M-H] $^-$) was also formed. (iii) In the pathway III, the cleavage of C = O bond and -OH in benzene ring occurred due to the attack of 1O_2 , forming the intermediate of p-ethylaminophenone $m/z-136b$ [M-H] $^-$. The intermediate of p-aminobenzoquinone ($m/z-107a$ [M-H] $^-$) was created as the attack of 1O_2 onto the 7 N-8C bond. The further attack on 4C-7 N bond formed the p-benzoquinone ($m/z-107b$ [M-H] $^-$), which would be degraded into the carboxylic acid and further converted into CO_2 and H_2O . As a result, the degradation intermediates as well as the pathways were consistent with the Fukui function values of f^+ and f^- (indicating the atom activities of PCM by the attack of $O_2^{\cdot-}$ and 1O_2).

4. Conclusions

An environmentally friendly, facile, and economical carbonaceous material (Fe-N@C) was prepared by simple thermal treatment of *Enteromorpha* biomass and the intrinsic N/Fe in *Enteromorpha* was co-doped into the carbon layers of the catalyst. SEM and TEM images

indicated the forms of graphitic nanosheets in the Fe-N@C with N and Fe well distributed. High graphitic N fractions derived from the intrinsic N in *Enteromorpha* and other biomass were observed, which showed the high correlation with the PCM removal rate. In contrast, intrinsic Fe in *Enteromorpha* did not affect the PCM degradation. The radical pathways involving $\text{SO}_4^{\cdot-}$ and $\cdot\text{OH}$ only donated a very small contribution to the PCM removal. In contrast, both the radical pathways of $\text{O}_2^{\cdot-}$ and non-radical $^1\text{O}_2$ activated in the Fe-N@C/PMS system were the primary pathways for the PCM degradation. Complete degradation of PCM still could be achieved after three consecutive runs and PCM removal rate of used Fe-N@C was mostly recovered (k : 0.1142 min^{-1}) after heat regeneration (500°C). All these results indicated the high stability and reusability of Fe-N@C for PMS activation. Adsorption energies (ΔE_{ads}) of PMS molecular adsorbed onto the graphitic N area was -2.62 eV based on the DFT calculation, which indicated that the graphitic N can activate PMS via enhancing PMS adsorption on the catalysts. In addition, different pathways for PCM degradation were involved considering the radical attack ($\text{O}_2^{\cdot-}$) and electrophilic attack ($^1\text{O}_2$), which were confirmed by the DFT calculations.

Conflicts of interest

There are no conflicts to declare.

Acknowledgements

The research was supported by China Postdoctoral Science Foundation funded project (2014M560556, 2015T80721). This work was also supported by grants from Tai Shan Scholar Foundation (No. ts201511003), Key Research Projects of Shandong Province (No. 2017GSF17109) and 2018WLJH52.

Appendix A. Supplementary data

Supplementary material related to this article can be found, in the online version, at doi:<https://doi.org/10.1016/j.apcatb.2019.03.048>.

References

- Z. Yao, W. Jiao, F. Shao, H. Song, H. Zhang, Q. Zhou, A. Li, Fabrication and characterization of amphiphilic magnetic water purification materials for efficient PPCPs removal, *Chem. Eng. J.* 360 (2019) 511–518.
- L. Ma, Y. Liu, J. Zhang, Q. Yang, G. Li, D. Zhang, Impacts of irrigation water sources and geochemical conditions on vertical distribution of pharmaceutical and personal care products (PPCPs) in the vadose zone soils, *Sci. Total Environ.* 626 (2018) 1148–1156.
- A. Li, Z. Wu, T. Wang, S. Hou, B. Huang, X. Kong, X. Li, Y. Guan, R. Qiu, J. Fang, Kinetics and mechanisms of the degradation of PPCPs by zero-valent iron (Fe^0) activated peroxydisulfate (PDS) system in groundwater, *J. Hazard. Mater.* 357 (2018) 207–216.
- G. Li, X. Nie, Y. Gao, T. An, Can environmental pharmaceuticals be photocatalytically degraded and completely mineralized in water using g-C₃N₄/TiO₂ under visible light irradiation?—Implications of persistent toxic intermediates, *Appl. Catal. B: Environ.* 180 (2016) 726–732.
- T. An, H. Yang, G. Li, W. Song, W.J. Cooper, X. Nie, Kinetics and mechanism of advanced oxidation processes (AOPs) in degradation of ciprofloxacin in water, *Appl. Catal. B: Environ.* 94 (2010) 288–294.
- J. Zur, D. Wojcieszynska, K. Hupert-Kocurek, A. Marchlewicz, U. Guzik, Paracetamol – toxicity and microbial utilization. *Pseudomonas moorei* KB4 as a case study for exploring degradation pathway, *Chemosphere* 206 (2018) 192–202.
- T.M. Attia, Effect of paracetamol/prednisolone versus paracetamol/ibuprofen on post-operative recovery after adult tonsillectomy, *Am. J. Otolaryngol.* 39 (2018) 476–480.
- D.W. Kolpin, E.T. Furlong, M.T. Meyer, E.M. Thurman, S.D. Zaugg, L.B. Barber, H.T. Buxton, Pharmaceuticals, hormones, and other organic wastewater contaminants in U.S. streams, 1999–2000: a national reconnaissance, *Environ. Sci. Technol.* 36 (2002) 1202–1211.
- L. Yang, L.E. Yu, M.B. Ray, Degradation of paracetamol in aqueous solutions by TiO₂ photocatalysis, *Water Res.* 42 (2008) 3480–3488.
- M. Cantarella, A. Di Mauro, A. Gulino, L. Spitaleri, G. Nicotra, V. Privitera, G. Impellizzeri, Selective photodegradation of paracetamol by molecularly imprinted ZnO nanonuts, *Appl. Catal. B: Environ.* 238 (2018) 509–517.
- Y. Yuan, D. Zhao, J. Li, F. Wu, M. Brigante, G. Mailhot, Rapid oxidation of paracetamol by Cobalt(II) catalyzed sulfite at alkaline pH, *Catal. Today* 313 (2018) 155–160.
- Y. Qin, L. Zhang, T. An, Hydrothermal carbon-mediated fenton-like reaction mechanism in the degradation ofalachlor: direct electron transfer from hydrothermal carbon to Fe(III), *ACS Appl. Mater. Interfaces* 9 (2017) 17115–17124.
- Y. Qin, G. Li, Y. Gao, L. Zhang, Y.S. Ok, T. An, Persistent free radicals in carbon-based materials on transformation of refractory organic contaminants (ROCs) in water: a critical review, *Water Res.* 137 (2018) 130–143.
- F. Audino, L. Conte, A. Schenone, M. Pérez-Moya, M. Graells, O.M. Alfano, A kinetic study for the fenton and photo-Fenton paracetamol degradation in a pilot plant reactor, in: A. Espuña, M. Graells, L. Puigjaner (Eds.), *Computer Aided Chemical Engineering*, Elsevier, 2017, pp. 301–306.
- X. Duan, C. Su, J. Miao, Y. Zhong, Z. Shao, S. Wang, H. Sun, Insights into perovskite-catalyzed peroxymonosulfate activation: maneuverable cobalt sites for promoted evolution of sulfate radicals, *Appl. Catal. B: Environ.* 220 (2018) 626–634.
- Y. Wang, S. Zhao, W. Fan, Y. Tian, X. Zhao, The synthesis of novel Co–Al₂O₃ nanofibrous membranes with efficient activation of peroxymonosulfate for bisphenol A degradation, *Environ. Sci.: Nano* 5 (2018) 1933–1942.
- G.X. Huang, C.Y. Wang, C.W. Yang, P.C. Guo, H.Q. Yu, Degradation of bisphenol A by peroxymonosulfate catalytically activated with Mn_{1.8}Fe_{1.2}O₄ nanospheres: synergism between Mn and Fe, *Environ. Sci. Technol.* 51 (2017) 12611–12618.
- Y.Y. Ahn, E.T. Yun, J.W. Seo, C. Lee, S.H. Kim, J.H. Kim, J. Lee, Activation of peroxymonosulfate by surface-loaded noble metal nanoparticles for oxidative degradation of organic compounds, *Environ. Sci. Technol.* 50 (2016) 10187–10197.
- H. Li, C. Shan, B.C. Pan, Fe(III)-doped g-C₃N₄ mediated activation of peroxymonosulfate for selective degradation of phenolic compounds via high valent iron-oxo species, *Environ. Sci. Technol.* 52 (2018).
- Y. Wang, Z. Ao, H. Sun, X. Duan, S. Wang, Activation of peroxymonosulfate by carbonaceous oxygen groups: experimental and density functional theory calculations, *Appl. Catal. B: Environ.* 198 (2016) 295–302.
- M. Xie, J. Tang, L. Kong, W. Lu, V. Natarajan, F. Zhu, J. Zhan, Cobalt doped g-C₃N₄ activation of peroxymonosulfate for monochlorophenols degradation, *Chem. Eng. J.* 360 (2018) 1213–1222.
- P. Liang, C. Zhang, X. Duan, H. Sun, S. Liu, M.O. Tade, S. Wang, An insight into metal organic framework derived N-doped graphene for the oxidative degradation of persistent contaminants: formation mechanism and generation of singlet oxygen from peroxymonosulfate, *Environ. Sci. Nano* 4 (2017).
- S. Zhu, X. Huang, F. Ma, L. Wang, X. Duan, S. Wang, Catalytic removal of aqueous contaminants on N-doped graphitic biochars: inherent roles of adsorption and nonradical mechanisms, *Environ. Sci. Technol.* 52 (2018) 8649–8658.
- A. Bonilla-Petriciolet, D. Mendoza-Castillo, H. Reynel, Adsorption Processes for Water Treatment and Purification, (2017).
- J. Zhou, Z. Lou, K. Yang, J. Xu, Y. Li, Y. Liu, S.A. Baig, X. Xu, Electrocatalytic dechlorination of 2,4-dichlorobenzoic acid using different carbon-supported palladium moveable catalysts: adsorption and dechlorination activity, *Appl. Catal. B: Environ.* 244 (2019) 215–224.
- W. Tian, H. Zhang, Z. Qian, T. Ouyang, H. Sun, J. Qin, M.O. Tade, S. Wang, Bread-making synthesis of hierarchically Co/C nanoarchitecture in heteroatom doped porous carbons for oxidative degradation of emerging contaminants, *Appl. Catal. B: Environ.* 225 (2018) 76–83.
- W. Tian, H. Zhang, H. Sun, M.O. Tade, S. Wang, One-step synthesis of flour-derived functional nanocarbons with hierarchical pores for versatile environmental applications, *Chem. Eng. J.* 347 (2018) 432–439.
- C. Wang, J. Kang, P. Liang, H. Zhang, H. Sun, M.O. Tade, S. Wang, Ferric carbide nanocrystals encapsulated in nitrogen-doped carbon nanotubes as an outstanding environmental catalyst, *Environ. Sci. Nano* 4 (2017) 170–179.
- T. Zhang, X. Yue, L. Gao, F. Qiu, J. Xu, J. Rong, J. Pan, Hierarchically porous bismuth oxide/layered double hydroxide composites: preparation, characterization and iodine adsorption, *J. Clean. Prod.* 144 (2017) 220–227.
- Y. Long, S. Bu, Y. Huang, Y. Shao, L. Xiao, X. Shi, N-doped hierarchically porous carbon for highly efficient metal-free catalytic activation of peroxymonosulfate in water: a non-radical mechanism, *Chemosphere* 216 (2019) 545–555.
- Y. Yao, H. Chen, C. Lian, F. Wei, D. Zhang, G. Wu, B. Chen, S. Wang, Co Fe, Ni nanocrystals encapsulated in nitrogen-doped carbon nanotubes as Fenton-like catalysts for organic pollutant removal, *J. Hazard. Mater.* 314 (2016) 129–139.
- W. Chen, H. Yang, Y. Chen, M. Xia, X. Chen, H. Chen, Transformation of nitrogen and evolution of N-containing species during algae pyrolysis, *Environ. Sci. Technol.* 51 (2017) 6570–6579.
- B. Su, B. Ge, M. Li, Y. Chen, Y. Chen, J. Zhang, H. Chen, J. Li, Extraction, characterization and deoxy-liquefaction of crude polysaccharide from *Enteromorpha prolifera* to high-quality liquid oil, *Fuel* 237 (2019) 763–768.
- Y. Zhao, J. Nin, D. Shang, M. Zhai, Analysis of inorganic elements of *Enteromorpha prolifera* from Qingdao coasts in 2008, *J. Biol.* 27 (2010) 92–93.
- J. Mahmood, F. Li, C. Kim, H.-J. Choi, O. Gwon, S.-M. Jung, J.-M. Seo, S.-J. Cho, Y.-W. Ju, H.Y. Jeong, G. Kim, J.-B. Baek, Fe@C₂N: a highly-efficient indirect-contact oxygen reduction catalyst, *Nano Energy* 44 (2018) 304–310.
- J. Kang, X. Duan, C. Wang, H. Sun, X. Tan, M.O. Tade, S. Wang, Nitrogen-doped bamboo-like carbon nanotubes with Ni encapsulation for persulfate activation to remove emerging contaminants with excellent catalytic stability, *Chem. Eng. J.* 332 (2018) 398–408.
- W. Ma, N. Wang, Y. Du, T. Tong, L. Zhang, Kun-Yi Andrew Lin, X. Han, One-step synthesis of novel Fe₃C@nitrogen-doped carbon nanotubes/graphene nanosheets for catalytic degradation of Bisphenol A in the presence of peroxymonosulfate, *Chem. Eng. J.* 356 (2019) 1022–1031.
- X. Duan, Z. Ao, L. Zhou, H. Sun, G. Wang, S. Wang, Occurrence of radical and nonradical pathways from carbocatalysts for aqueous and nonaqueous catalytic oxidation, *Appl. Catal. B: Environ.* 188 (2016) 98–105.

- [39] X. Duan, H. Sun, Z. Shao, S. Wang, Nonradical reactions in environmental remediation processes: uncertainty and challenges, *Appl. Catal. B: Environ.* 224 (2018) 973–982.
- [40] W. Ma, N. Wang, Y. Du, P. Xu, B. Sun, L. Zhang, K.-Y.A. Lin, Human-hair-derived N, S-doped porous carbon: an enrichment and degradation system for wastewater remediation in the presence of peroxymonosulfate, *ACS Sustain. Chem. Eng.* 7 (2019) 2718–2727.
- [41] P. Sun, H. Liu, Z. Zhai, X. Zhang, Y. Fang, J. Tan, J. Wu, Degradation of UV filter BP-1 with nitrogen-doped industrial graphene as a metal-free catalyst of peroxymonosulfate activation, *Chem. Eng. J.* 356 (2019) 262–271.
- [42] R. Luo, M. Li, C. Wang, M. Zhang, M.A. Nasir Khan, X. Sun, J. Shen, W. Han, L. Wang, J. Li, Singlet oxygen-dominated non-radical oxidation process for efficient degradation of bisphenol A under high salinity condition, *Water Res.* 148 (2019) 416–424.
- [43] X. Duan, H. Sun, S. Wang, Metal-free carbocatalysis in advanced oxidation reactions, *Acc. Chem. Res.* 51 (2018) 678–687.
- [44] Y. Feng, C. Liao, L. Kong, D. Wu, Y. Liu, P.-H. Lee, K. Shih, Facile synthesis of highly reactive and stable Fe-doped g-C₃N₄ composites for peroxymonosulfate activation: a novel nonradical oxidation process, *J. Hazard. Mater.* 354 (2018) 63–71.
- [45] C. Li, J. Wu, W. Peng, Z. Fang, J. Liu, Peroxymonosulfate activation for efficient sulfamethoxazole degradation by Fe₃O₄/β-FeOOH nanocomposites: coexistence of radical and non-radical reactions, *Chem. Eng. J.* 356 (2019) 904–914.
- [46] J. Miao, X. Duan, J. Li, J. Dai, B. Liu, S. Wang, W. Zhou, Z. Shao, Boosting performance of lanthanide magnetism perovskite for advanced oxidation through lattice doping with catalytically inert element, *Chem. Eng. J.* 355 (2019) 721–730.
- [47] L. Tang, Y. Liu, J. Wang, G. Zeng, Y. Deng, H. Dong, H. Feng, J. Wang, B. Peng, Enhanced activation process of persulfate by mesoporous carbon for degradation of aqueous organic pollutants: electron transfer mechanism, *Appl. Catal. B: Environ.* 231 (2018) 1–10.
- [48] C. Qi, X. Liu, J. Ma, C. Lin, X. Li, H. Zhang, Activation of peroxymonosulfate by base: implications for the degradation of organic pollutants, *Chemosphere* 151 (2016) 280–288.
- [49] J. Wang, S. Wang, Activation of persulfate (PS) and peroxymonosulfate (PMS) and application for the degradation of emerging contaminants, *Chem. Eng. J.* 334 (2018) 1502–1517.
- [50] G.-L. Li, G.-C. Cheng, W.-W. Chen, C.-D. Liu, L.-F. Yuan, B.-B. Yang, C. Hao, N/S/B-doped graphitized carbon encased Fe species as a highly active and durable catalyst towards oxygen reduction reaction, *J. Colloid Interface Sci.* 514 (2018) 108–116.
- [51] A.A. Gorman, M.A.J. Rodgers, Singlet molecular-oxygen, *Chem. Soc. Rev.* 10 (1981) 205–231.
- [52] S. Zhu, X. Li, J. Kang, X. Duan, S. Wang, Persulfate activation on crystallographic manganese oxides: mechanism of singlet oxygen evolution for nonradical selective degradation of aqueous contaminants, *Environ. Sci. Technol.* 53 (2019) 307–315.
- [53] F. Guo, K. Wang, J. Lu, J. Chen, X. Dong, D. Xia, A. Zhang, Q. Wang, Activation of peroxymonosulfate by magnetic carbon supported Prussian blue nanocomposite for the degradation of organic contaminants with singlet oxygen and superoxide radicals, *Chemosphere* 218 (2019) 1071–1081.
- [54] X. Zhang, L. Zhang, Z. Li, Z. Jiang, Q. Zheng, B. Lin, B. Pan, Rational design of antifouling polymeric nanocomposite for sustainable fluoride removal from NOM-rich water, *Environ. Sci. Technol.* 51 (2017) 13363–13371.
- [55] Y. Zhou, J. Jiang, Y. Gao, J. Ma, S.-Y. Pang, J. Li, X.-T. Lu, L.-P. Yuan, Activation of peroxymonosulfate by benzoquinone: a novel nonradical oxidation process, *Environ. Sci. Technol.* 49 (2015) 12941–12950.
- [56] P.H. Shao, J.Y. Tian, F. Yang, X.G. Duan, S.S. Gao, W.X. Shi, X.B. Luo, F.Y. Cui, S.L. Luo, S.B. Wang, Identification and regulation of active sites on nanodiamonds: establishing a highly efficient catalytic system for oxidation of organic contaminants, *Adv. Funct. Mater.* 28 (2018) 8.
- [57] E.-T. Yun, G.-H. Moon, H. Lee, T.H. Jeon, C. Lee, W. Choi, J. Lee, Oxidation of organic pollutants by peroxymonosulfate activated with low-temperature-modified nanodiamonds: understanding the reaction kinetics and mechanism, *Appl. Catal. B: Environ.* 237 (2018) 432–441.
- [58] Y. Wang, M. Liu, X. Zhao, D. Cao, T. Guo, B. Yang, Insights into heterogeneous catalysis of peroxymonosulfate activation by boron-doped ordered mesoporous carbon, *Carbon* 135 (2018) 238–247.
- [59] L. Lyu, G. Yu, L. Zhang, C. Hu, Y. Sun, 4-Phenoxyphenol-functionalized reduced graphene oxide nanosheets: a metal-free fenton-like catalyst for pollutant destruction, *Environ. Sci. Technol.* 52 (2018) 747–756.
- [60] L. Wang, J. Jiang, S.-Y. Pang, Y. Zhou, J. Li, S. Sun, Y. Gao, C. Jiang, Oxidation of bisphenol A by nonradical activation of peroxymonosulfate in the presence of amorphous manganese dioxide, *Chem. Eng. J.* 352 (2018) 1004–1013.
- [61] J. Cui, L. Zhang, B. Xi, J. Zhang, X. Mao, Chemical oxidation of benzene and trichloroethylene by a combination of peroxymonosulfate and permanganate linked by in-situ generated colloidal/amorphous MnO₂, *Chem. Eng. J.* 313 (2017) 815–825.
- [62] X. Li, X. Liu, C. Lin, H. Zhang, Z. Zhou, G. Fan, M. He, W. Ouyang, Activation of peroxymonosulfate by magnetic catalysts derived from drinking water treatment residuals for the degradation of atrazine, *J. Hazard. Mater.* 366 (2019) 402–412.
- [63] L. Chen, X. Zuo, S. Yang, T. Cai, D. Ding, Rational design and synthesis of hollow Co₃O₄@Fe₂O₃ core-shell nanostructure for the catalytic degradation of norfloxacin by coupling with peroxymonosulfate, *Chem. Eng. J.* 359 (2019) 373–384.
- [64] X. Duan, C. Su, L. Zhou, H. Sun, A. Suvorova, T. Odedairo, Z. Zhu, Z. Shao, S. Wang, Surface controlled generation of reactive radicals from persulfate by carbocatalysis on nanodiamonds, *Appl. Catal. B: Environ.* 194 (2016) 7–15.
- [65] D. Xia, Y. Li, G. Huang, R. Yin, T. An, G. Li, H. Zhao, A. Lu, P.K. Wong, Activation of persulfates by natural magnetic pyrrhotite for water disinfection: efficiency, mechanisms, and stability, *Water Res.* 112 (2017) 236–247.
- [66] Y.-H. Guan, J. Ma, Y.-M. Ren, Y.-L. Liu, J.-Y. Xiao, L.-q. Lin, C. Zhang, Efficient degradation of atrazine by magnetic porous copper ferrite catalyzed peroxymonosulfate oxidation via the formation of hydroxyl and sulfate radicals, *Water Res.* 47 (2013) 5431–5438.
- [67] T. An, J. An, Y. Gao, G. Li, H. Fang, W. Song, Photocatalytic degradation and mineralization mechanism and toxicity assessment of antiviral drug acyclovir: experimental and theoretical studies, *Appl. Catal. B: Environ.* 164 (2015) 279–287.
- [68] X. Chen, W.-D. Oh, T.-T. Lim, Graphene- and CNTs-based carbocatalysts in persulfates activation: material design and catalytic mechanisms, *Chem. Eng. J.* 354 (2018) 941–976.
- [69] R. Yin, W. Guo, H. Wang, J. Du, X. Zhou, Q. Wu, H. Zheng, J. Chang, N. Ren, Enhanced peroxymonosulfate activation for sulfamethazine degradation by ultrasound irradiation: performances and mechanisms, *Chem. Eng. J.* 335 (2018) 145–153.
- [70] R. Zhang, X. Wang, L. Zhou, Z. Liu, D. Crump, The impact of dissolved oxygen on sulfate radical-induced oxidation of organic micro-pollutants: a theoretical study, *Water Res.* 135 (2018) 144–154.
- [71] A.-M. Abdel-Wahab, A.-S. Al-Shirbini, O. Mohamed, O. Nasr, Photocatalytic degradation of paracetamol over magnetic flower-like TiO₂/Fe₂O₃ core-shell nanostructures, *J. Photochem. Photobiol. A: Chem.* 347 (2017) 186–198.
- [72] S. Slamani, F. Abdelmalek, M.R. Ghezzer, A. Addou, Initiation of Fenton process by plasma gliding arc discharge for the degradation of paracetamol in water, *J. Photochem. Photobiol. A: Chem.* 359 (2018) 1–10.
- [73] A.G. Trovó, R.F. Pupo Nogueira, A. Agüera, A.R. Fernandez-Alba, S. Malato, Paracetamol degradation intermediates and toxicity during photo-Fenton treatment using different iron species, *Water Res.* 46 (2012) 5374–5380.
- [74] L. Rimoldi, D. Meroni, E. Falletta, A.M. Ferretti, A. Gervasini, G. Cappelletti, S. Ardizzone, The role played by different TiO₂ features on the photocatalytic degradation of paracetamol, *Appl. Surf. Sci.* 424 (2017) 198–205.